Progress In Electromagnetics Research M, Vol. 138, 55–64, 2026

PIER M

(Received 26 March 2026, Accepted 25 May 2026, Scheduled 12 June 2026)

Broadband and Switchable VO_2-Based Bi-Functional THz Polarization Converter Combined with a Deep-Learning-Assisted Design Method

Haohan Xie[1], Shuning Wei[1], Wenting Qu[1], Xinlei Zhang[1], Chenshan Le[1], Jinlin Li[2], and Jun Dong[1,*]

[1] *College of Information Science and Engineering, Hunan Normal University, Changsha 410081, China*
[2] *Fujian Provincial Key Laboratory of Terahertz Functional Devices and Intelligent Sensing*
Fuzhou University, Fuzhou 350108, China

ABSTRACT: This study presents a broadband, switchable, and bifunctional terahertz device based on the phase transition of vanadium dioxide (VO_2). When VO_2 is in the metallic state, the device operates as a linear polarization converter (LPC). When VO_2 transitions to the insulating state, the device functions as a broadband linear-to-circular polarization converter (LTC-PC). Numerical simulations are conducted to verify the device performance. To further optimize metamaterial performance and accelerate the design process, a deep learning framework that integrates convolutional neural networks (CNNs) and the Transformer architecture via an adaptive mechanism is proposed. Numerical simulations indicate that this LPC achieves a polarization conversion ratio (PCR) exceeding 90% across the 1.92–2.93 THz band and maintains angular stability for incidence angles up to 50°. The LTC-PC operates effectively within the 2.40–4.33 THz range. Featuring broadband operation and bi-functional capabilities, the converter holds significant potential for applications in terahertz imaging, sensing, solar energy harvesting, and communications.

1. INTRODUCTION

The terahertz (THz) region (0.1–10 THz), which bridges the microwave and optical frequencies, offers transformative potential in terahertz imaging [1], sensors [2], multiband devices [3], and anomalous reflection [4]. Despite these promising uses, the application of THz systems has long been hindered by the intrinsic limitations of conventional materials, particularly their inability to support dynamic reconfigurability. Driven by these challenges, planar artificial subwavelength metamaterials have emerged as promising platforms for THz-wave manipulation through geometric-phase control and resonant-element design [5–13]. However, those metamaterial devices remain incapable of dynamic functionality switching on their own and still rely on external modulation schemes, resulting in increased system complexity and restricted practicality [14].

To address this limitation, a promising pathway to intrinsic reconfigurability lies in integrating tunable materials, such as graphene [15–17], vanadium dioxide (VO_2) [18], and graphene-VO_2 hybrids [19, 20], into metamaterial architectures, where their externally tunable electromagnetic properties enable dynamic control of the overall response. Among them, VO_2 exhibits a near-room-temperature insulator-metal transition that induces drastic changes in its electrical and optical properties [21–24]. This enables the metamaterial to switch electromagnetic states and overcome the bandwidth and angular limitations of conventional metamaterial designs. VO_2-based metamaterials exhibit multifunctional characteristics and can integrate multiple electromagnetic responses, including absorption [25], switchable bi-functional absorption and polarization conversion [26–28]. Using VO_2, researchers have achieved broadband absorption switching across different frequency bands [25], a multifunctional metamaterial enabling simultaneous absorption and polarization conversion [27], and a switch between perfect absorption and polarization conversion [26], all of which demonstrate its multifunctional capability. Moreover, graphene-VO_2 hybrids have demonstrated switchable linear-to-linear and reflective linear-to-circular polarization conversion [29], which increases the functional diversity and integration of devices. However, the use of multiple materials in a device introduces complexity to its design.

In this study, we propose a broadband bifunctional polarization-conversion device based on VO_2 as a single material, leveraging its phase-transition characteristics to achieve dynamic polarization manipulation. When VO_2 is metallic, the device acts as a high-efficiency linear polarization converter, achieving a polarization conversion ratio exceeding 90% from 1.92 to 2.93 THz with angular stability of up to 50°. In the insulating state, it functions as a broadband linear-to-circular polarization converter, capable of converting linear polarization to circular polarization over the 2.40–4.33 THz band. This design enables future applications in polarization-sensitive imaging, adaptive radar systems, and solar energy harvesting.

Recently, deep learning has been employed in the design of electromagnetic devices to significantly improve the opti-

---

* Corresponding author: Jun Dong (jdongcn@outlook.com).

doi:10.2528/PIERM26032606

Published by THE ELECTROMAGNETIC ACADEMY

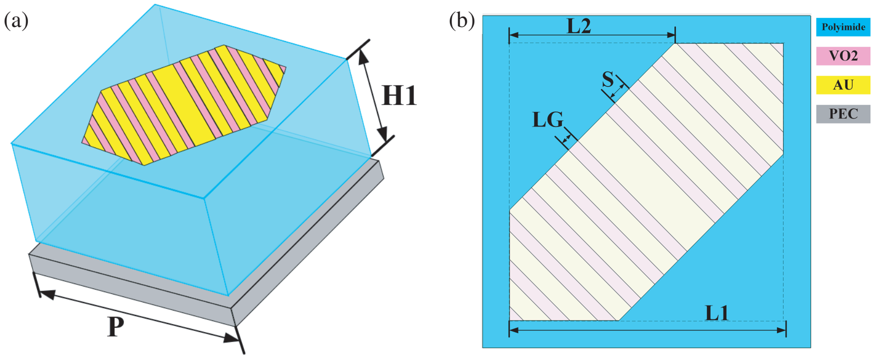

FIGURE 1. Schematic of the designed metamaterial.

mization efficiency [30, 31]. To accelerate the design process and address the computational challenges inherent in traditional metamaterial design methodologies, this study introduces a hybrid CNN-Transformer architecture that constructs an end-to-end mapping between geometric parameters and electromagnetic responses, thereby enabling efficient design optimization.

2. DESIGN OF SWITCHABLE POLARIZATION CONVERTER

2.1. The Proposed Converter: Structure and Simulation

Figure 1 illustrates the schematic configuration of the three-dimensional reflective polarization converter and its unit cell. The designed structure comprises three vertically stacked layers: a reflective ground plane at the bottom, a polyimide dielectric spacer in the middle, and a patterned gold layer and VO_2 film at the top. The top plane consists of periodically arranged alternating gold and VO_2 strips, which are oriented at a 45° angle to the incident wave polarization. This configuration ensures the total reflection of the incident waves and enables efficient cross-polarization conversion. The unit cell of the proposed metamaterial consists of a periodic arrangement of gold and VO_2 strips, avoiding the complex curves or disconnected features found in conventional designs, such as spirals, dual rings, or ginkgo-leaf patterns.

The terahertz frequency dielectric characteristics of VO_2 were appropriately modeled using the Drude formalism [32].

$$\varepsilon_{\mathrm{VO}_2}(\omega) = \varepsilon_\infty - \frac{\omega_p^2 \sigma_{\mathrm{VO}_2}}{\omega^2 + i\gamma\omega} \tag{1}$$

Here, $\varepsilon_\infty = 12$ denotes the permittivity at high frequencies. The plasma frequency is expressed as:

$$\omega_p^2(\sigma_{\mathrm{VO}_2}) = \left(\frac{\sigma_{\mathrm{VO}_2}}{\sigma_0}\right) \omega_p^2(\sigma_0) \tag{2}$$

with $\omega_p(\sigma_0) = 1.4 \times 10^{15}$ rad/s. Additionally, $\gamma = 5.75 \times 10^{13}$ rad/s represents the damping rate, and the conductivity at the reference state is $\sigma_0 = 3 \times 10^5$ S/m. VO_2 is a temperature-sensitive material that transitions from an insulator to a metal at a critical temperature of approximately 340 K.

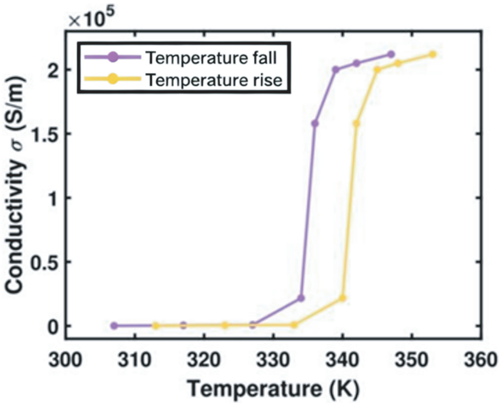

FIGURE 2. The conductivity of VO_2 as a function of temperature extracted from data presented in [32].

As illustrated in Fig. 2, VO_2 is a prime example of a material exhibiting thermally activated phase transitions [32]. Under ambient conditions, it exists as an insulating monoclinic crystal. Upon heating past its transition point, it reversibly transforms into a metallic tetragonal rutile phase, with electrical conductivity increasing by 3–5 orders of magnitude. This unique switching property makes VO_2 highly valuable for applications in reconfigurable electronics, smart metamaterials, and terahertz modulation [26].

In simulations, VO_2 was modeled in two distinct phase states, considering both the conductive and dielectric states, whereas the gold constituent maintained a fixed electrical conductance value of 4.561×10^7 S/m. The dielectric spacer was fabricated from biphenyl tetracarboxylic polyimide, exhibiting a dielectric constant $\varepsilon_r = 3.5$ and a dissipation factor $\tan\delta = 0.027$. The computational domain settings employed periodic boundary constraints along the lateral (x) and longitudinal (y) axes, with radiation-absorbing boundaries implemented along the vertical axis. A linearly polarized terahertz wavefront was configured to propagate along the negative vertical axis. As shown in Fig. 1, parametric optimization procedures established the optimal geometric parameters as follows: lattice period $P = 30\,\mu\text{m}$, metallic strips with longitudinal dimensions $L1 = 25\,\mu\text{m}$ and $L2 = 15\,\mu\text{m}$, VO_2 channel width $LG = 1.2\,\mu\text{m}$ interspersed with separation gaps $S = 1.8\,\mu\text{m}$, dielectric elevations $H1 = 10.0\,\mu\text{m}$, and stratum thickness parameters $t1 = 1\,\mu\text{m}$.

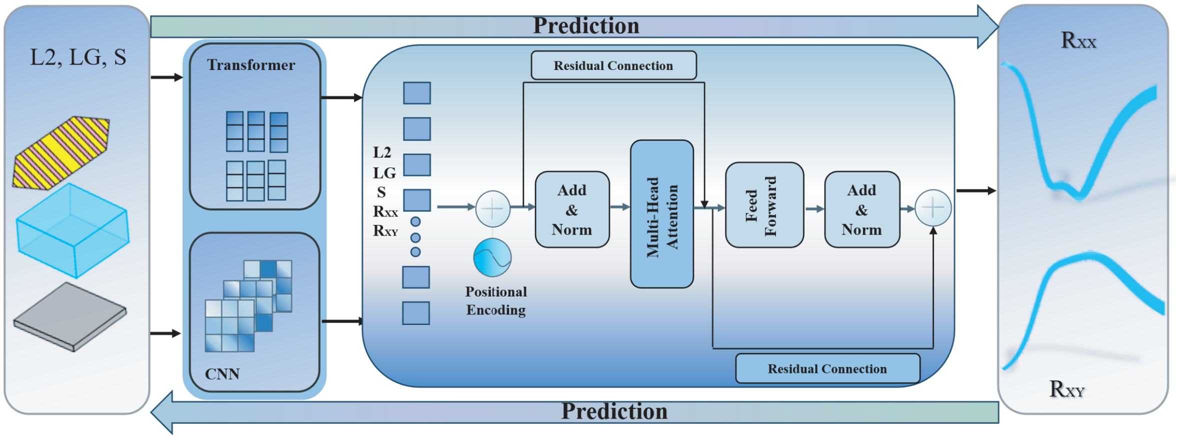

FIGURE 3. Deep learning schematic.

2.2. Hybrid Deep Learning Architecture for Accelerated Design

This study establishes a deep-learning-driven electromagnetic prediction framework to optimize the broadband and switchable performance of the proposed VO_2-based terahertz metamaterial converter. As depicted in Fig. 3, the framework employs a hybrid neural network that integrates Convolutional Neural Networks (CNNs) and transformer architectures through an adaptive mechanism, enabling end-to-end mapping between structural parameters and electromagnetic responses. The model directly predicts the reflection spectra corresponding to different VO_2 phase states, thereby eliminating the need for the time-consuming iterative computations typical of conventional full-wave simulations [33].

During data building, both the geometric parameters of the metamaterial unit ($L2$, LG, and S) and their corresponding electromagnetic responses (R_{xx}, R_{xy}) were normalized to the [0, 1] range to ensure stable convergence and balanced feature scaling. Within the hybrid model, the CNN module captures local spatial correlations and fine-grained geometric dependencies, which are essential for accurately describing sub wavelength electromagnetic interactions in the converter design. The Transformer encoder, equipped with multi-head self-attention, learns global feature dependencies and adaptively emphasizes the most relevant structural features.

During training, a simulated annealing-based optimization strategy was used to identify the optimal learning rate, in conjunction with the Adam optimizer and a dynamic learning rate scheduler adjusted according to the validation performance. This data-driven approach enables the rapid and accurate prediction of the polarization conversion characteristics of in both metallic and insulating states of VO_2, significantly reducing computational costs and accelerating the metamaterial design process.

3. RESULTS AND DISCUSSION

3.1. Design result of the Linear Polarization Converter

In the metallic phase of VO_2, the device exhibits functionality as a linear polarization converter. To quantitatively evaluate polarization conversion efficiency, and the PCR metric is employed, serving as a critical performance indicator for the converter system.

$$\mathrm{PCR} = \frac{|r_{yx}|^2}{|r_{xx}|^2 + |r_{yx}|^2} \tag{3}$$

The complex reflection coefficients for the cross-polarized and co-polarized wave components are denoted as r_{xy} and r_{xx}, respectively. Using x-polarized incidence as a representative case, numerical simulations were performed to evaluate the polarization conversion characteristics under positive z-axis propagation. Figs. 4(a) and (b) present the computational outcomes of the co-polarized reflection coefficients, cross-polarized reflection coefficients, and PCR metrics for the broadband terahertz metamaterial linear polarization converter. Numerical analysis revealed that across the 1.92–2.93 THz spectral range, PCR magnitudes exceeded 90.00%, indicating that over 90.00% of the reflected electromagnetic energy corresponded to cross-polarized components. These findings demonstrate the device's capability to execute high-efficiency linear-polarization conversion across a 1.01 THz operational bandwidth centered at 2.425 THz.

A parametric influence analysis was conducted to evaluate the effect of parameters on polarization conversion performance. The dielectric spacer thickness $H1$ was systematically modulated in 1.0 µm increments across 8–12 µm. Computational simulations generated PCR and ellipticity frequency responses corresponding to different $H1$ values, as illustrated in Fig. 4(c).

The analysis revealed progressive bandwidth contraction and a leftward frequency shift in high-PCR regions with increasing $H1$ magnitudes. The optimal performance was identified at $H1 = 10.0$ µm. Complementary investigations in Fig. 4(d) demonstrate that the metallic element length $L2$ exerts a negligible influence on the PCR relative to other variables, with comprehensive optimization selecting $L2 = 15.0$ µm as the preferred configuration.

The angular dependence of polarization orientation and incidence angle on PCR was analyzed. As shown in Fig. 5(a), PCR is fully suppressed at 45°, while peak conversion appears

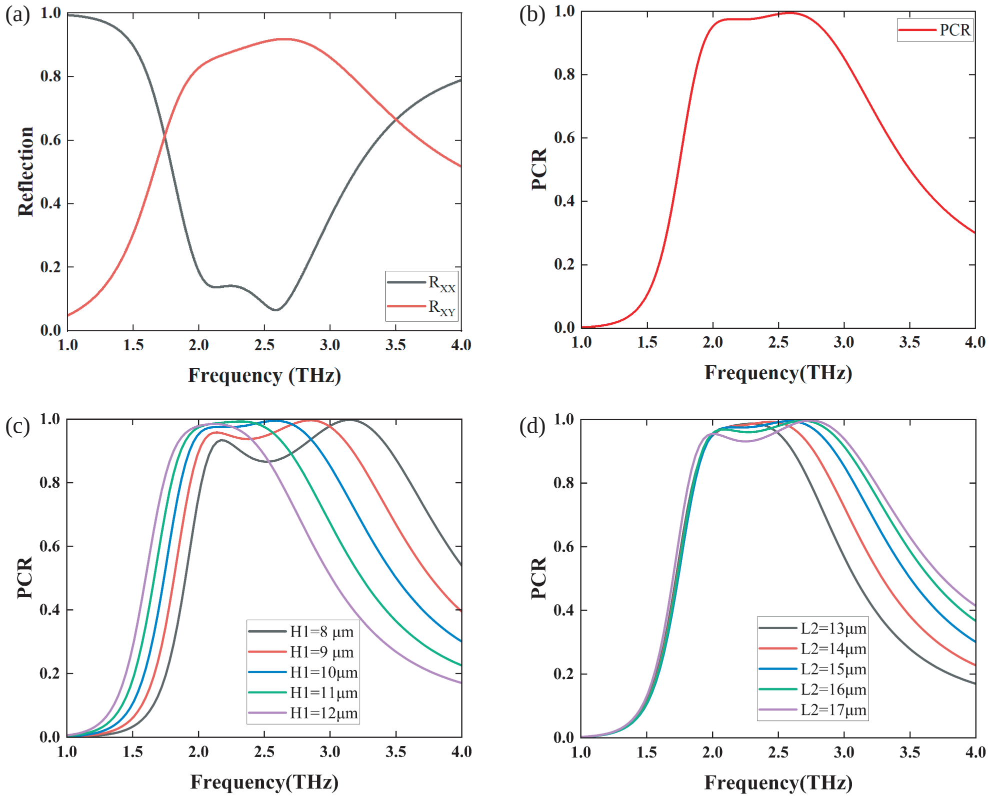

FIGURE 4. (a) Co-polarized and cross-polarized reflection coefficient amplitudes, (b) PCR, (c) the PCR for different heights $H1$, and (d) the PCR for different metallic lengths $L2$.

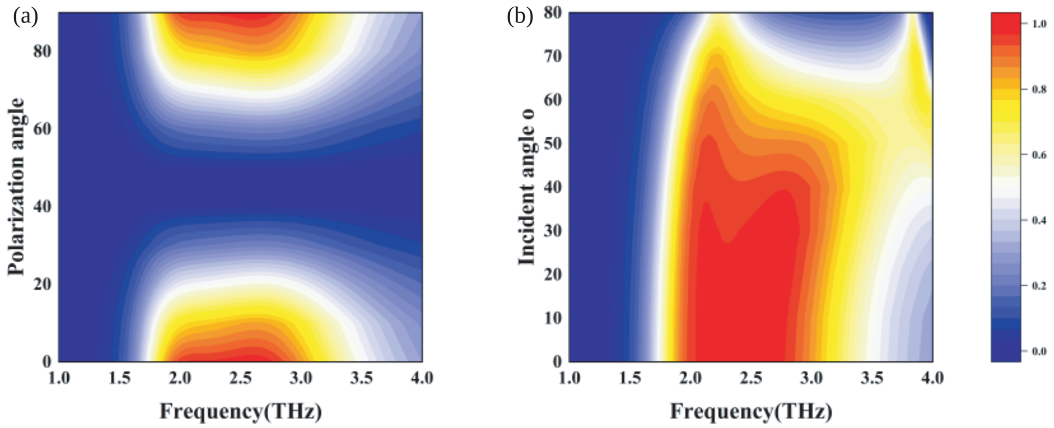

FIGURE 5. (a) Relationship between polarization angle and cross-polarization conversion ratio at vertical incidence, (b) The relationship between the incident angle and the cross-polarization conversion ratio.

at 0° (x-polarization) and 90° (y-polarization). Fig. 5(b) shows that PCR remains above 90% for incidence angles up to 50°, confirming high efficiency and angular insensitivity. These results validate the polarization-dependent characteristics of the converter.

3.2. Design Result of the Linear-to-Circular Polarization Converter

In the insulating state, the VO_2 device acts as a linear-to-circular polarization converter. Simulations were performed using the Finite Integration Technique with periodic boundaries. Due to the structure's diagonal symmetry, analysis was restricted to y-polarized incidence. The incident and reflected electric field components are formulated as follows:

$$\vec{E}_i = E_{xi}\hat{x} + E_{yi}\hat{y} \tag{4}$$

$$\vec{E}_r = E_{xr}\hat{x} + E_{yr}\hat{y} \tag{5}$$

The electromagnetic field vectors associated with incoming and reflected radiation along the orthogonal axes are denoted by $E_{xi}(E_{xr})$ and $E_{yi}(E_{yr})$, corresponding to the x- and y-

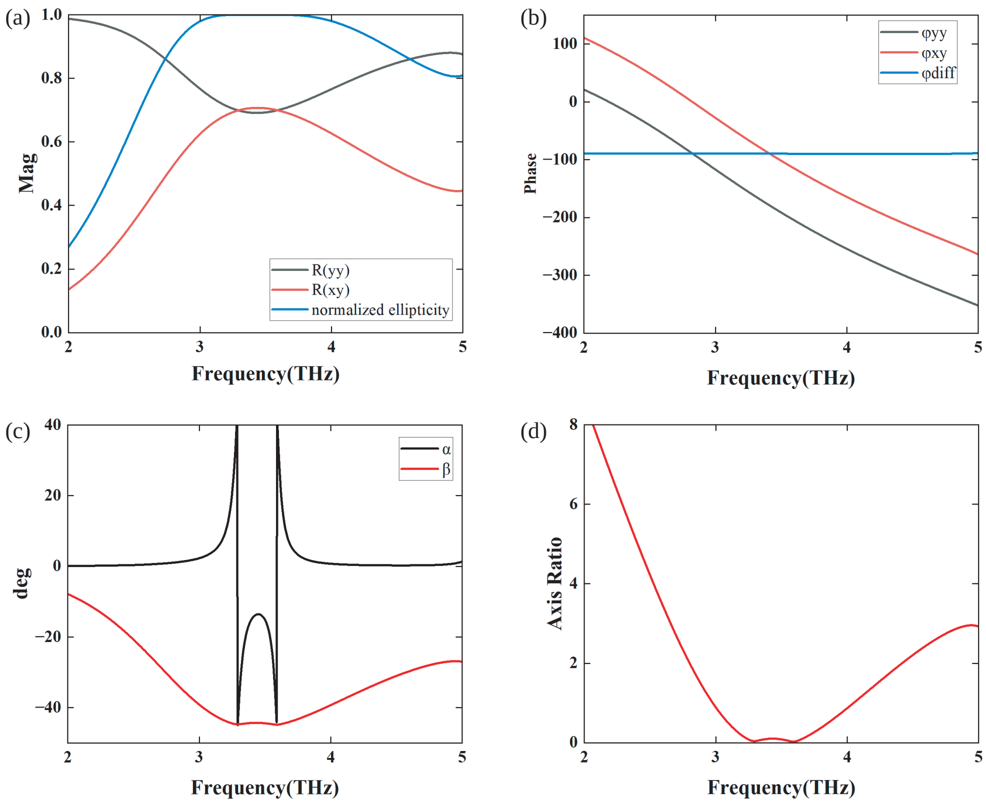

FIGURE 6. (a) Spectral responses of reflection coefficients and normalized ellipticity, (b) phase of R_{yy}, R_{xy}, and their difference, (c) polarization azimuth α and ellipticity angles β, and (d) axial ratio performance metrics.

directional components, respectively. The reflected electromagnetic wavefront can be mathematically represented as:

$$\vec{E}_r = \sum_{i=x,y} R_{yi} \cdot e^{-j(kz-\phi_{yi})} \cdot E_{yi} \cdot \hat{y}_i \tag{6}$$

In this context, R_{xy} and R_{yy} are defined as the reflection coefficients corresponding to the co-polarized and cross-polarized components, respectively. The phase difference between these components is mathematically expressed as:

$$\phi_{diff} = \phi_{xy} - \phi_{yy} \tag{7}$$

As illustrated in Figs. 6(a) and (b), the reflection coefficients R_{xy} and R_{yy} exhibit comparable magnitudes while maintaining a phase difference $\phi_{diff} \approx -90^\circ$ across the 2.40–4.33 THz spectral regime. Meanwhile, the normalized ellipticity (χ), which functions as a metric for evaluating the linear-to-circular polarization conversion efficiency, attains values approaching unity within this frequency band. This numerical evidence indicates the generation of a near-ideal right-handed circularly polarized reflection. The χ parameter approaching 1.0 highlights the exceptional ultra-wideband operational characteristics of the LTC-PC.

The normalized ellipticity is mathematically defined through the following relationship, where $A = R_{yy}$, $B = R_{xy}$, and $C = \phi_{diff}$:

$$\chi = 2 \cdot \frac{AB}{A^2 + B^2} \cdot \sin(c) \tag{8}$$

To characterize the polarization state transformation in the reflected electromagnetic waves, the Stokes parameters are used according to the following formulation [34]:

$$I = A^2 + B^2 \tag{9}$$

$$Q = A^2 - B^2 \tag{10}$$

$$U = 2AB \cdot \cos(c) \tag{11}$$

$$V = 2AB \cdot \sin(c) \tag{12}$$

To further analyze the circular polarization reflection field, we introduce the polarization azimuth angle (α) and ellipticity angle (β), as expressed in the following equation [35]:

$$\alpha = \frac{1}{2} \arctan \left[\frac{U}{Q} \right] \tag{13}$$

$$\beta = \frac{1}{2} \arcsin \left[\frac{V}{I} \right] \tag{14}$$

Axial ratio (AR) is an important parameter for evaluating the performance of a circular polarization converter and is mathematically defined as follows [17]:

$$AR = 10 \cdot \log_{10} (\tan(\beta)) \tag{15}$$

In this study, we analyze the orientation of the ellipse using the parameter α, defined as the ellipse's deviation from the principal axis. The parameter effectively captures the ellipse's deviation from a standard circle. As depicted in Fig. 6(c), a 45° angular alignment was observed at 3.29 and 3.58 THz, indicating a nearly circular polarization state. Consequently, the

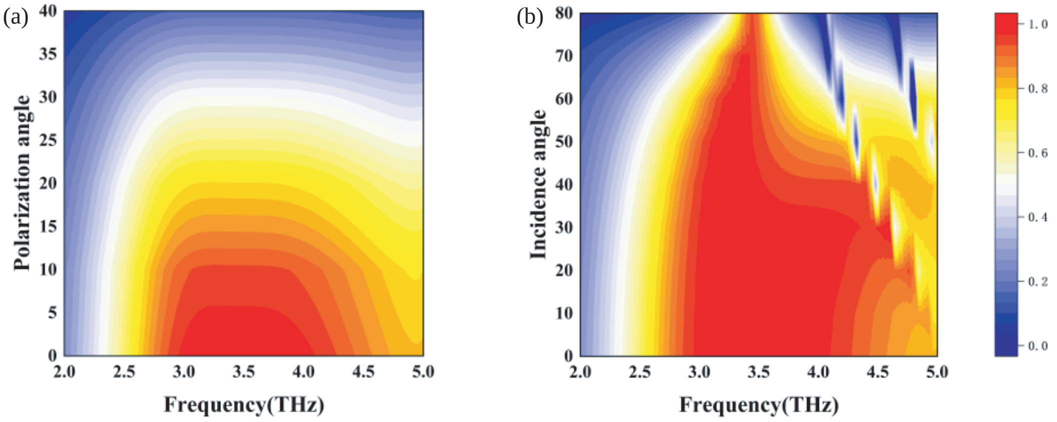

FIGURE 7. (a)–(b) The performance of the PC when the polarization angle.

TABLE 1. Performance comparison of bi-functional device.

Ref.	Tunable material	Conversion mode	Bandwidth of LPC		Bandwidth of LTC-PC	
			Fre. Range (THz)	Relative bandwidth (%)	Fre. Range (THz)	Relative Bandwidth (%)
[15]	Graphene	LTC-PC	/	/	2.30–4.0	54
[16]	Graphene	LPC	10.4–21.5	69.62	/	/
[29]	Graphene and VO_2	LPC LTC-PC	0.36–0.53	38.6	0.38–0.7	57.1
[26]	VO_2	LTC-PC	/	/	1.47–2.27	42.7
[27]	VO_2	LPC	1.42.1	40	/	/
This work	VO_2	LPC LTC-PC	1.92–2.93	41.65	2.40–4.33	57.36

reflected wavefront exhibited near-circular polarization properties, deviating slightly from the ideal circular polarization characteristics. Fig. 6(d) illustrates that within the frequency ranges of 2.40–4.33 THz, the AR is less than 3 dB.

The angular performance of the converter was evaluated. Fig. 7(a) shows the LTC-PC efficiency for y-LP radiation with the polarization orientation from 0° to 40°. Fig. 7(b) plots normalized ellipticity versus incidence angle, which remains above 0.8 over 0°–40°. Notably, ellipticity strongly depends on the polarization orientation of incident y-LP waves.

As shown in Table 1, our proposed design achieves a relative bandwidth of 41.65% for LPC and 57.36% for LTC-PC. Compared to other dual-functional devices, such as the graphene-VO_2-based design in [29], our work offers competitive bandwidth performance. Furthermore, it demonstrates distinct advantages over single-functional converters reported in [15, 16, 26, 27] by successfully integrating both conversion modes into a single tunable structure.

3.3. Deep Learning for Parameter Optimization

CNN is a widely used deep learning architecture designed for grid-structured data, such as images and sequences. In this study, the CNN module functioned as a local feature extractor, capturing the key relationships among the geometric parameters. Although the inputs ($L2$, LG, S) are provided as one-dimensional vectors, the one-dimensional CNN effectively learns the local interactions and parameter combinations that influence the electromagnetic response, such as resonance sharpness and bandwidth. The use of a one-dimensional convolutional structure allows the model to extract continuous geometric dependencies while remaining computationally efficient. For a one-dimensional input sequence $X \in \mathbb{R}^L$ (where L is the sequence length), convolved with a convolutional kernel $K \in \mathbb{R}^L$ (where k is the kernel size), the i element of the output feature map $Y \in \mathbb{R}^L$ is calculated as:

$$Y_i = (X * K)_i = \sum_{j=1}^{k} X_{i+j-1} \cdot K_j + b \tag{16}$$

The symbol $*$ represents the convolution operation, and b denotes the bias term. Using multiple convolution kernels, the network can learn various local features in parallel.

As shown in Fig. 8, the CNN module encodes the three input geometric parameters ($L2$, LG, and S) into a set of features rich in local information, denoted as FCNN, providing high-quality inputs for the subsequent transformer module. The transformer is a neural network architecture based on the self-attention mechanism that completely abandons recurrent and

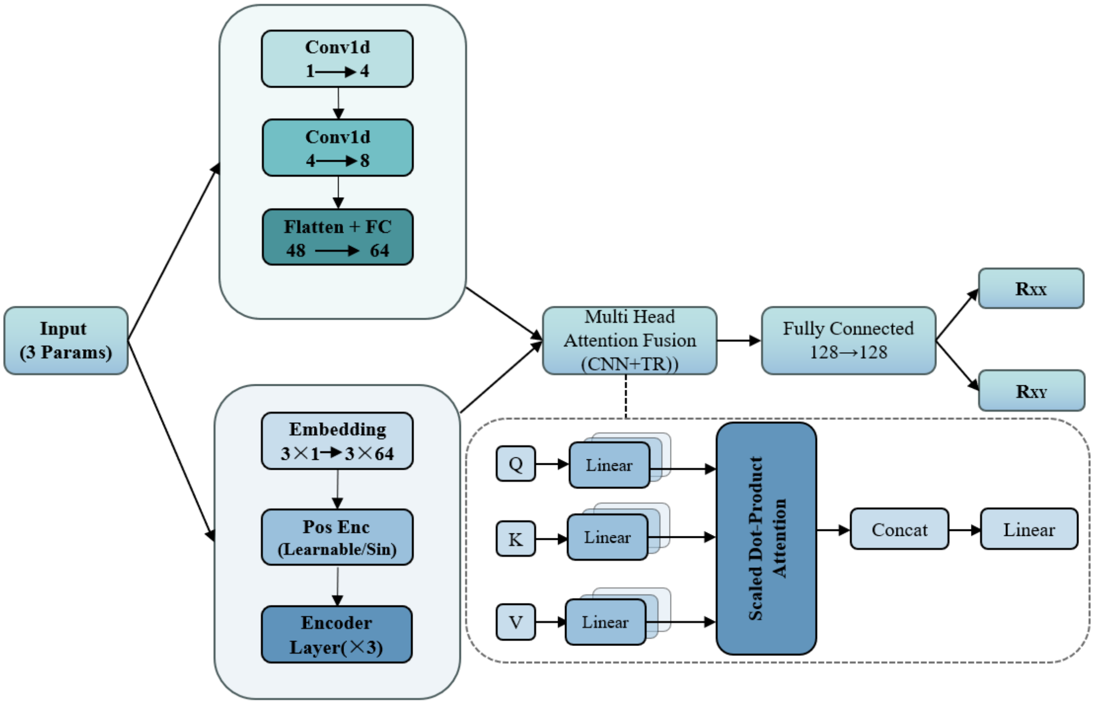

FIGURE 8. Neural network architecture schematic.

convolutional structures and excels at capturing long-range dependencies in sequential data. In this study, the role of the transformer encoder module is to capture global parameter dependencies. It receives the feature sequence extracted from the CNN and analyzes the correlation among all feature elements via the self-attention mechanism, thereby understanding how any two geometric parameters influence each other and jointly determine the final electromagnetic response. The core of the self-attention mechanism is the query-key-value (QKV) model. The input feature matrix FCNN is first projected into three spaces: query (Q), key (K), and value (V) through linear transformations [36].

$$Q = F_{\text{CNN}} W^Q, \quad K = F_{\text{CNN}} W^K, \quad V = F_{\text{CNN}} W^V \tag{17}$$

In this context, $W^Q, W^K, W^V \in \mathbb{R}^{d \times d_k}$ represent the learnable weight matrices. The attention weights are derived from the dot product of queries and keys, followed by scaling and normalization via the Softmax function. The specific formula is as follows:

$$\text{Attention}(Q, K, V) = \text{softmax}\left(\frac{QK^T}{\sqrt{d_k}}\right) V \tag{18}$$

The scaling factor $\sqrt{d_k}$ is used to prevent the dot product result from becoming excessively large, which could cause the gradient of the Softmax function to vanish. To enhance the model's expressive power across different representational subspaces, the transformer employs a multi-head attention mechanism. It projects Q, K, V into h distinct subspaces, computes attention in parallel, and then concatenates and projects the results back to the original dimension.

$$\text{MultiHead}(Q, K, V) = \text{Concat}(\text{head}_1, \text{head}_2, \ldots, \text{head}_h) W^O \tag{19}$$

$$\text{where } \text{head}_i = \text{Attention}(Q W_i^Q, K W_i^K, V W_i^V) \tag{20}$$

In this study, the multi-head mechanism allows the model to simultaneously capture multiple dependencies from different parameters. For example, one head focuses on the effect of S on coupling, while another head attends to the influence of $L2$ on the global phase, thus more comprehensively modeling the complex physical relationships between input parameters and output electromagnetic responses.

The models were trained on a server equipped with an NVIDIA A800 GPU. The implementation was done in PyTorch, using Python 3.8. A total of 500 data samples were generated via full-wave electromagnetic simulations, and the dataset was randomly split into training, validation, and test sets with a ratio of 8 : 1 : 1. Training was performed for 1000 epochs with a batch size of 32, employing the AdamW optimizer and ReduceLROnPlateau scheduler.

As shown in Fig. 9, the deep learning model achieves highly accurate fitting of R_{xx} and R_{xy} in both the training and testing sets, with predicted results closely consistent with the target values. This demonstrates that the model effectively captures the inherent relationships within the data and provides highly accurate and reliable prediction results. The model shows no overfitting or underfitting, and can accurately characterize the key features and their internal correlations. With its precise modeling capability and strong generalization performance, the proposed model can be effectively applied to the optimal design of polarization converters. It can rapidly determine the optimal device geometry and realize excellent polarization conversion performance.

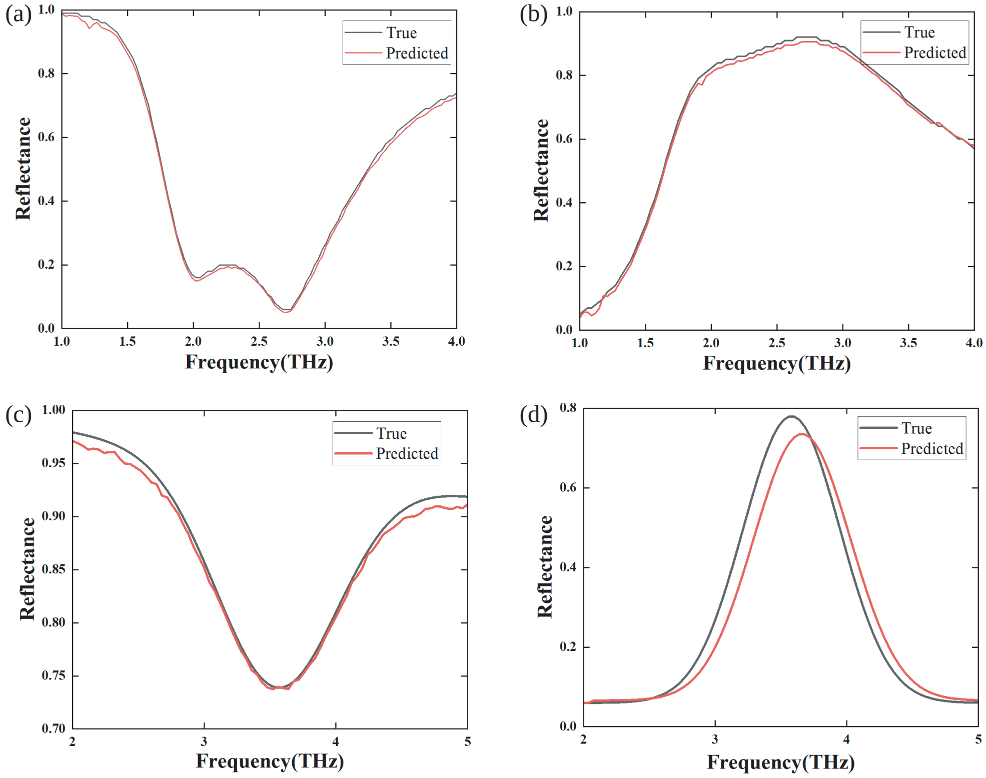

FIGURE 9. (a) and (b) show the testing and training results of r_{xx} and r_{xy} under linear polarization. (c) and (d) display the testing and training results of r_{xx} and r_{xy} under circular polarization.

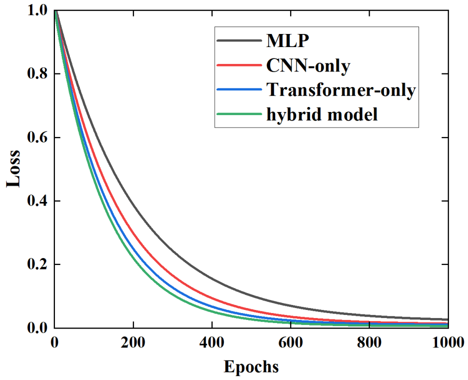

FIGURE 10. Training loss comparison of MLP, CNN-only, Transformer-only, and hybrid CNN-Transformer models.

TABLE 2. Comparison of mean absolute error (MAE) and mean square error (MSE) metrics for different models.

	R_{yy} MAE	R_{xy} MAE	R_{yy} MSE	R_{xy} MSE
MLP	0.002814	0.003050	0.000012	0.000012
CNN-only	0.002861	0.003121	0.000012	0.000012
Transformer-only	0.02982	0.03415	0.000013	0.000014
Hybrid	0.003188	0.003870	0.000015	0.000029

As shown in Fig. 10, the hybrid model exhibits faster convergence and achieves lower final training loss than MLP, CNN-only, and Transformer-only models. This performance suggests that the hybrid architecture more effectively captures the underlying features of the data.

As listed in Table 2, the proposed hybrid CNN-Transformer model yields competitive prediction errors within the same order of magnitude as the baselines, while demonstrating significantly faster convergence as shown in Fig. 10.

4. CONCLUSION

This study demonstrates a bi-functional terahertz metamaterial device based on VO_2. When VO_2 is in the metallic state, the metamaterial functions as an efficient linear polarization converter, achieving polarization conversion ratios exceeding 90% over the 1.92–2.93 THz band while maintaining stable performance at incidence angles up to 50°. Following the phase transition to the insulating state, the metamaterial transitions into a broadband linear-to-circular polarization conversion system. In the frequency range of 2.40 to 4.33 THz, linearly polarized electromagnetic waves can be effectively converted into circularly polarized electromagnetic waves with an axial ratio of less than 3 dB. Compared with existing active terahertz polarization converters, the proposed device exhibits broader bandwidth and greater functional versatility.

The device is developed using a deep learning framework that integrates CNN with Transformer. This model effectively learns both local and global correlations among geometric parameters. It achieves high prediction accuracy and enables efficient discovery of structures exhibiting broadband performance. These results confirm the strong potential of deep-learning-driven strategies for intelligent terahertz metamaterial design. The proposed converter offers new opportunities for terahertz imaging, spectrum management, solar energy modulation, and next-generation radar communications.

ACKNOWLEDGEMENT

This work was supported in part by the Open Project Program of Fujian Provincial Key Laboratory of Terahertz Functional Devices and Intelligent Sensing, China under No. FPKLTFDIS202303, the Open Project of Xiangjiang Laboratory under grant No. 25XJ03019, Hunan Province Degree and Graduate Education Reform Research Project under Grant No. 2023JGYB115, Hunan Province College Students Research Learning And Innovative Experiment Project under Grant No. S202410542270, S202410542052X, and Hunan Normal University Open Access Fund for Large Instrumentation Testing under Grant No. 25CSZ002, 25CSZ004, 25CSY022, 25CSY023, and 25CSY024.

REFERENCES

[1] Jansen, C., S. Wietzke, O. Peters, M. Scheller, N. Vieweg, M. Salhi, N. Krumbholz, C. Jördens, T. Hochrein, and M. Koch, “Terahertz imaging: Applications and perspectives,” *Applied Optics*, Vol. 49, No. 19, E48–E57, 2010.

[2] Xu, J., D. Liao, M. Gupta, Y. Zhu, S. Zhuang, R. Singh, and L. Chen, “Terahertz microfluidic sensing with dual-torus toroidal metasurfaces,” *Advanced Optical Materials*, Vol. 9, No. 15, 2100024, 2021.

[3] Bhattacharya, A., R. Sarkar, N. K. Sharma, B. K. Bhowmik, A. Ahmad, and G. Kumar, “Multiband transparency effect induced by toroidal excitation in a strongly coupled planar terahertz metamaterial,” *Scientific Reports*, Vol. 11, No. 1, 19186, 2021.

[4] Sreekanth, K. V., M. ElKabbash, Y. Alapan, A. R. Rashed, U. A. Gurkan, and G. Strangi, “A multiband perfect absorber based on hyperbolic metamaterials,” *Scientific Reports*, Vol. 6, No. 1, 26272, 2016.

[5] Monticone, F. and A. Alù, “Metamaterial, plasmonic and nanophotonic devices,” *Reports on Progress in Physics*, Vol. 80, No. 3, 036401, 2017.

[6] Paniagua-Domínguez, R., Y. F. Yu, E. Khaidarov, S. Choi, V. Leong, R. M. Bakker, X. Liang, Y. H. Fu, V. Valuckas, L. A. Krivitsky, and A. I. Kuznetsov, “A metalens with a near-unity numerical aperture,” *Nano Letters*, Vol. 18, No. 3, 2124–2132, 2018.

[7] Bhowmik, B. K., L. K. Vaswani, A. Panwar, M. Tigala, A. Kumar, and G. Kumar, “Polarization-independent electromagnetically induced transparency in a bound state in continuum assisted terahertz metamolecule,” *Journal of Infrared, Millimeter, and Terahertz Waves*, Vol. 46, No. 10, 67, 2025.

[8] Luo, H., Y. Xiong, Y. Cheng, F. Chen, and X. Li, “Optical transparent metamaterial structure for microwave-infrared-compatible camouflage based on indium tin oxide,” *Science China Technological Sciences*, Vol. 66, No. 10, 2850–2861, 2023.

[9] You, X., R. T. Ako, M. Bhaskaran, S. Sriram, C. Fumeaux, and W. Withayachumnankul, “Mechanically tunable terahertz circular polarizer with versatile functions,” *Laser & Photonics Reviews*, Vol. 17, No. 4, 2200305, 2023.

[10] Zhao, J., N. Li, and Y. Cheng, “Ultrabroadband chiral metasurface for linear polarization conversion and asymmetric transmission based on enhanced interference theory,” *Chinese Optics Letters*, Vol. 21, No. 11, 113602, 2023.

[11] Deng, M., S. Kanwal, Z. Wang, C. Cai, Y. Cheng, J. Guan, G. Hu, J. Wang, J. Wen, and L. Chen, “Dielectric metasurfaces for broadband phase-contrast relief-like imaging,” *Nano Letters*, Vol. 24, No. 46, 14 641–14 647, 2024.

[12] You, X., R. T. Ako, S. Sriram, and W. Withayachumnankul, “3D terahertz confocal imaging with chromatic metasurface,” *Laser & Photonics Reviews*, Vol. 19, No. 7, 2401011, 2025.

[13] Liu, M., L. Yang, C. Cao, X. Cao, Y. Cheng, H. Luo, F. Chen, and X. Li, “Switchable narrowband/broadband terahertz metasurface absorber based on single-layer graphene structure,” *Diamond and Related Materials*, Vol. 161, 113199, 2026.

[14] Guo, G., X. Zhang, L. Niu, T. Wu, X. Chen, Q. Xu, J. Han, and W. Zhang, “Programmable graphene metasurface for terahertz propagation control based on electromagnetically induced transparency,” *Carbon*, Vol. 208, 345–354, 2023.

[15] Mistri, H., A. Ghosh, A. R. Sardar, and B. Choudhury, “Performance enhancement of graphene-based linear to circular polarization converter for terahertz frequency using a novel parameter prediction methodology,” *Plasmonics*, Vol. 20, No. 6, 3289–3303, 2025.

[16] Sheheryar, T., X. Dong, X. Wang, B. Lv, L. Gao, and B. Xie, “High-efficiency graphene-based terahertz polarization converter with integrated biological sensing and tunable performance,” *ACS Applied Optical Materials*, Vol. 3, No. 10, 2384–2398, 2025.

[17] Barkabian, M., N. Sharifi, and N. Granpayeh, “Multi-functional high-efficiency reflective polarization converter based on an ultra-thin graphene metasurface in the THz band,” *Optics Express*, Vol. 29, No. 13, 20 160–20 174, 2021.

[18] Budai, J. D., J. Hong, M. E. Manley, E. D. Specht, C. W. Li, J. Z. Tischler, D. L. Abernathy, A. H. Said, B. M. Leu, L. A. Boatner, R. J. McQueeney, and O. Delaire, “Metallization of vanadium dioxide driven by large phonon entropy,” *Nature*, Vol. 515, No. 7528, 535–539, 2014.

[19] Li, D., S. He, L. Su, H. Du, Y. Tian, Z. Gao, B. Xie, and G. Huang, “Switchable and tunable terahertz metamaterial absorber based on graphene and vanadium dioxide,” *Optical Materials*, Vol. 147, 114655, 2024.

[20] Wang, X., C. Ma, L. Xiao, and B. Xiao, “Dual-band dynamically tunable absorbers based on graphene and double vanadium dioxide metamaterials,” *Journal of Optics*, Vol. 53, No. 1, 596–604, 2024.

[21] Morin, F. J., “Oxides which show a metal-to-insulator transition at the neel temperature,” *Physical Review Letters*, Vol. 3, No. 1, 34, 1959.

[22] Zhao, W., X. Lv, Q. Xu, Z. Wen, Y. Shao, C. Liu, and N. Dai, “Multifunctional terahertz metamaterials device based on a dual-tunable structure incorporating graphene and vanadium oxide,” *Nanoscale Advances*, Vol. 7, No. 12, 3817–3827, 2025.

[23] Liu, L., L. Kang, T. S. Mayer, and D. H. Werner, “Hybrid metamaterials for electrically triggered multifunctional control,” *Nature Communications*, Vol. 7, No. 1, 13236, 2016.

[24] Hilton, D. J., R. P. Prasankumar, S. Fourmaux, A. Cavalleri, D. Brassard, M. A. E. Khakani, J. C. Kieffer, A. J. Taylor, and R. D. Averitt, “Enhanced photosusceptibility near T_c for the light-induced insulator-to-metal phase transition in vanadium dioxide,” *Physical Review Letters*, Vol. 99, No. 22, 226401, 2007.

[25] Zhao, Y., Q. Huang, H. Cai, X. Lin, and Y. Lu, "A broadband and switchable VO_2-based perfect absorber at the THz frequency," *Optics Communications*, Vol. 426, 443–449, 2018.

[26] Yan, D., M. Meng, J. Li, J. Li, and X. Li, "Vanadium dioxide-assisted broadband absorption and linear-to-circular polarization conversion based on a single metasurface design for the terahertz wave," *Optics Express*, Vol. 28, No. 20, 29 843–29 854, 2020.

[27] Wang, F., J. Cui, H. Liu, T. Ma, X. Wang, and Y. Liu, "Terahertz metamaterial devices with switchable absorption and polarization conversion based on vanadium dioxide," *Progress In Electromagnetics Research C*, Vol. 153, 61–70, 2025.

[28] He, H., X. Shang, L. Xu, J. Zhao, W. Cai, J. Wang, C. Zhao, and L. Wang, "Thermally switchable bifunctional plasmonic metasurface for perfect absorption and polarization conversion based on VO_2," *Optics Express*, Vol. 28, No. 4, 4563–4570, 2020.

[29] Feng, J.-L., L.-S. Wu, and J.-F. Mao, "Broadband terahertz multifunctional polarization converter based on a hybrid metasurface with graphene and vanadium dioxide," in *2022 IEEE MTT-S International Microwave Workshop Series on Advanced Materials and Processes for RF and THz Applications (IMWS-AMP)*, 1–3, Guangzhou, China, 2022.

[30] Cui, L., K. Huang, Y. Zhong, Y. Zhang, and Q. H. Liu, "An auxiliary classifier generative method for antenna design and optimization," *IEEE Transactions on Antennas and Propagation*, Vol. 73, No. 2, 733–747, 2025.

[31] Rong, C., L. Wu, L. Yang, B. Cai, Y. Cheng, F. Chen, H. Luo, and X. Li, "Deep learning enabled inverse design of terahertz chiral metasurface based on insb for dual-functional sensing," *Optics & Laser Technology*, Vol. 200, 115185, 2026.

[32] Barzegar-Parizi, S., A. Ebrahimi, and K. Ghorbani, "Two bits dual-band switchable terahertz absorber enabled by composite graphene and vanadium dioxide metamaterials," *Scientific Reports*, Vol. 14, No. 1, 5818, 2024.

[33] Neronha, J., H. Guerboukha, and D. M. Mittleman, "Using neural networks to design leaky-wave antennas for terahertz wireless links," *Journal of Infrared, Millimeter, and Terahertz Waves*, Vol. 46, No. 2, 14, 2025.

[34] Cong, L., W. Cao, X. Zhang, Z. Tian, J. Gu, R. Singh, J. Han, and W. Zhang, "A perfect metamaterial polarization rotator," *Applied Physics Letters*, Vol. 103, No. 17, 171107, 2013.

[35] Huang, C., X. Ma, M. Pu, G. Yi, Y. Wang, and X. Luo, "Dual-band 90° polarization rotator using twisted split ring resonators array," *Optics Communications*, Vol. 291, 345–348, 2013.

[36] Vaswani, A., N. Shazeer, N. Parmar, J. Uszkoreit, L. Jones, A. N. Gomez, Ł. Kaiser, and I. Polosukhin, "Attention is all you need," in *Advances in Neural Information Processing Systems*, Long Beach, CA, USA, 2017.